Macromolecules
ARTICLE

Macromolecules **2010**, *43*, 10045–10054 **10045**
DOI: 10.1021/ma101768b

Flow-Induced Ordering in Cubic Gels Formed by P2VP-*b*-PEO-*b*-P(GME-*co*-EGE) Triblock Terpolymer Micelles: A Rheo-SANS Study

Stefan Reinicke,[†] Matthias Karg,[‡] Alain Lapp,[§] Lutz Heymann,[∥] Thomas Hellweg,[⊥,○] and Holger Schmalz*[,†]

[†]*Makromolekulare Chemie II, Universität Bayreuth, D-95440 Bayreuth, Germany,*
[‡]*Bio21 Institute & School of Chemistry, University of Melbourne, 3010 Victoria, Australia,*
[§]*Laboratoire Léon Brillouin, CEA de Saclay, 99191 Gif sur Yvette, France,*
[∥]*Technische Mechanik und Strömungsmechanik, Universität Bayreuth, D-95440 Bayreuth, Germany,*
[⊥]*Physikalische Chemie I, Universität Bayreuth, D-95440 Bayreuth, Germany, and* [○]*Physikalische und Biophysikalische Chemie, Fakultät für Chemie, Universität Bielefeld, D-33615 Bielefeld, Germany*

Received August 3, 2010; Revised Manuscript Received October 28, 2010

ABSTRACT: Small-angle neutron scattering (SANS) measurements under steady shear were performed to determine the exact nature and degree of structural order within a hydrogel based on poly(2-vinylpyridine)-*block*-poly(ethylene oxide)-*block*-poly(glycidyl methyl ether-*co*-ethyl glycidyl ether) ($P2VP_{56}$-*b*-PEO_{410}-*b*-$P(GME_{48}$-*co*-$EGE_{48})$) triblock terpolymer micelles. Previous static SANS measurements indicated the presence of a simple cubic (sc) or body centered cubic (bcc) packing. By exposing the sample to steady shear, different macroscopic structural transitions were induced, indicated by a stress plateau and a significant change of the 2D SANS patterns. A comparison of these 2D patterns with patterns from analogous systems reported in literature and theoretical predictions revealed the presence of a bcc structure. Furthermore, with increasing shear rate the structural alignment changes from a nonoriented state to an intermediate state consisting of polycrystalline bcc domains with weak preferential orientation, and finally to a highly aligned state in which twinned bcc domains exist. The [111] axis of the twinned bcc crystals is aligned in the direction of the shear flow, and the {110} slipping planes are preferentially aligned parallel to the shear plane (walls of the Couette cell). A minor fraction of twinned bcc domains, probably located in regions of lower shear velocity, i.e., close to the inner wall of the Couette cell (stator), is tilted by an angle of 90° with respect to the shear plane.

Introduction

"Smart" hydrogels, i.e., networks of water-soluble polymers being sensitive to external stimuli like pH, temperature, light, or ionic strength, constitute a very active research field due to their versatility with respect to potential applications. "Smart" hydrogels can be utilized in biomedical applications like drug delivery and tissue engineering,[1−6] but also in sensors, storage media, actuating systems, or microfluidic devices.[7−11] In recent years, new concepts of "smart" hydrogels were established, mostly dealing with ABA, ABC, $(AB)_x$, and ABCBA type block copolymers. Here, the different blocks combine water solubility with stimuli-responsive behavior, and as a result physical network junctions can be reversibly formed and destroyed upon changes of an external stimulus.[12−18] Alternatively, chemically cross-linked hydrogels can swell or shrink, when different external parameters like temperature or pH are changed.[19−22]

Recently, we developed a new approach toward double stimuli-sensitive hydrogels, i.e., responding to both pH and temperature.[23,24] The physical hydrogels are based on ABC triblock terpolymers, which are composed of a water-soluble poly(ethylene oxide) (PEO) middle block, a pH-sensitive poly(2-vinylpyridine) (P2VP) A block, and a thermo-sensitive poly(glycidyl methyl ether-*co*-ethyl glycidyl ether) P(GME-*co*-EGE) C block. At pH = 7, core−shell−corona (CSC) micelles with a P2VP core, a PEO shell, and a thermo-sensitive corona composed of the P(GME-*co*-EGE) block are formed (Scheme 1).

*Corresponding author.

As an example, a $P2VP_{62}$-*b*-PEO_{452}-*b*-$P(GME_{36}$-*co*-$EGE_{36})$ triblock terpolymer (subscripts denote the number-average degree of polymerization of the corresponding block) undergoes a gel−sol−gel transition upon heating at concentrations higher than 12 wt %.[23] The high temperature gel state is formed via an open association of the CSC micelles, since the thermo-sensitive micellar corona collapses above the cloud point of the P(GME-*co*-EGE) block and forms the network junctions. The low temperature gel phase on the other hand is based on a close packing of CSC micelles. The form factor of the CSC micelles was extracted from small-angle neutron scattering (SANS) on dilute solutions at pH = 7, and could be fitted with a spherical core−shell model including additional Gaussian chains accounting for the soft corona. In concentrated solutions, a pronounced structure factor with higher order reflections at the relative peak positions of $1:2^{1/2}:3^{1/2}$ was observed, indicating an ordered cubic packing of the CSC micelles. Because of the absence of additional higher order reflections, a differentiation between a simple cubic (sc) or a body centered cubic (bcc) packing was not possible. However, the P2VP-*b*-PEO-*b*-P(GME-*co*-EGE) micelles have a relatively small P2VP core and a large, highly swollen PEO shell and P(GME-*co*-EGE) corona. Consequently, these micelles can be considered as "soft" spheres. In contrast to micelles with thin coronas (acting more or less like "hard" spheres), favoring a face centered cubic (fcc) structure,[25,26] "soft" spheres preferentially form a body centered cubic (bcc) structure. A bcc packing was reported for micelles based on different Pluronics type copolymers,[27−29] PEO end-capped with octadecyl groups at high concentration,[30] and polystyrene-*block*-polyisoprene/-polybutadiene (PS-*b*-PI/PS-*b*-PB) diblock

© 2010 American Chemical Society
Published on Web 11/11/2010

Scheme 1. Structure of the Studied P2VP$_{56}$-*b*-PEO$_{410}$-*b*-P(GME$_{48}$-*co*-EGE$_{48}$) Triblock Terpolymer and Formation of Core−Shell−Corona (CSC) Micelles in Water at pH = 7 and Room Temperature[a]

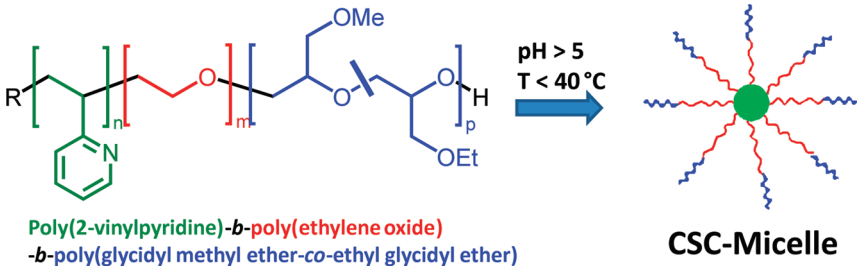

[a] Subscripts denote the number-average degree of polymerization of the corresponding block.

copolymers.[31−34] However, micelles acting as "soft" spheres often pack in a sc structure, too, as observed for poly(ethylene-*co*-propylene)-*block*-polydimethylsiloxane (PEP-*b*-PDMS),[35] poly(ethylene-*co*-propylene)-*block*-polystyrene (PEP-*b*-PS),[36] and PS-*b*-PB diblock copolymers in selective solvents.[37] Besides, systems were reported which can pack both in a fcc and a bcc structure, just depending on concentration and/or temperature. Such a behavior can be found for instance for a poly(ethylene oxide)-*block*-poly(butylene oxide) (PEO-*b*-PBO) diblock copolymer.[38] Additionally, Perreur et al. claimed that many differences in published interpretations of experimental data could be due to such fcc-bcc transitions.[27] Nevertheless, in most cases only one type of lattice is observed.

This work aims at the determination of the exact structure, i.e., sc or bcc, of a cubic gel formed by P2VP$_{56}$-*b*-PEO$_{410}$-*b*-P(GME$_{48}$-*co*-EGE$_{48}$) CSC micelles utilizing SANS measurements under steady shear, a frequently applied technique for studying block copolymer micellar gels.[27,28,34,38−43] The analysis of diffraction patterns of a sample under flow allows the assignment of the exact sample structure due to a macroscopic alignment of the polycrystalline domains. For this purpose, we prepared a sample with a concentration of 19 wt % (pH = 7) and performed SANS measurements at 20 °C during shear at various shear rates, as well as directly after cessation of the shear. The use of a Couette type shear cell geometry allowed us to record scattering patterns both in radial and tangential scattering geometry.

Experimental Section

Materials. The P2VP$_{56}$-*b*-PEO$_{410}$-*b*-P(GME$_{48}$-*co*-EGE$_{48}$) triblock terpolymer was synthesized via sequential anionic polymerization according to the procedure described elsewhere.[23,24] The triblock terpolymer exhibits a very narrow molecular weight distribution (PDI = 1.02), as determined by size exclusion chromatography using THF as eluent (PS calibration). D_2O (99.9%, Deutero GmbH), concentrated DCl (36−38% in D_2O, Deutero GmbH), and NaOD (40% in D_2O, Deutero GmbH) were used as received.

Sample Preparation. An 8 g sample of the triblock terpolymer was dissolved in 40 mL of D_2O. The apparent pH was adjusted to a value of 3−4 using concentrated DCl in order to protonate the P2VP block, rendering it hydrophilic. This ensures molecular dissolution of the polymer. The solution was then titrated slowly to $pH_{app} = 7$ (titer 1 M NaOD, dosing rate 1.3 μL min^{-1}), causing the deprotonation of the P2VP block, and consequently the formation of CSC micelles with a hydrophobic P2VP core. The apparent hydrodynamic radius of the CSC micelles is 23 nm with a polydispersity index of 0.14, as revealed by dynamic light scattering (ALV DLS/SLS-SP 5022F compact goniometer system with an ALV 5000/E cross-correlator and a He−Ne laser at $\lambda_0 =$ 632.8 nm, 1 g L^{-1}, $\theta = 90°$). The titrations and pH-measurements were performed using a titrator (Titrando 809, Metrohm, Herisau, Switzerland), equipped with a titration unit (Dosino 800, Metrohm, Herisau, Switzerland) and a common glass membrane pH-electrode (microelectrode, Metrohm, Herisau, Switzerland).

Rheology. Rheological experiments were performed using a Modular Compact Rheometer MCR500 (Anton Paar GmbH, Germany). For the temperature sweep under oscillatory shear, a truncated coaxial cone-and-plate geometry with a diameter $D =$ 25 mm, a cone angle $\beta = 1°$, and a minimum truncation gap $\kappa =$ 51 μm was employed. For the steady shear experiment, a coaxial cylinder system (Searle cell) having an outer radius $R_a = 5.4235$ mm, an inner radius $R_i = 5.00$ mm, and a gap length $L = 15$ mm was used. The lower end of the inner cylinder had a conical shape with an aperture of 120° in order to reduce end effects such as end face vortices at the end plane. Because of the small relative gap width $(R_a - R_i)/R_i = 0.0847$, the variation of the shear rate and shear stress in the gap can be assumed to be linearly dependent on the radial position, and independent of the material investigated. Hence, arithmetic mean values of shear rate and shear stress, calculated from the values at the inner and outer cylinder surface, could be used as representative values. The temperature was controlled with a precision of ±0.1 °C using a TEZ150P−C Peltier thermal unit for the coaxial cylinder geometry, and a TEK150P−C Peltier thermal unit for the cone-and-plate geometry in combination with a fluid bath thermostat VT2 (Julabo, Germany) for cooling. To avoid evaporation effects and axial temperature gradients, the Peltier thermal units were equipped with an insulating heated hood. Prior to all measurements, a four-step test and calibration procedure for the rheometer were performed, including measurement of the torque of the air bearing, detection of the inertia of the rheometer motor and the rotating part of the measurement systems, a careful calibration of the Peltier thermal units using calibrated thermal sensors (Ahlborn, Germany), and finally an accurate calibration with two certified Newtonian calibration liquids having viscosities of approximately 10^2 mPa·s and 10^4 mPa·s, respectively, at 20 °C.

In order to be able to load the sample (about 1.02 mL for the coaxial cylinder and 0.1 mL for the cone-and-plate geometry) easily into the corresponding measuring cell, both the cell and the sample were preheated to 40 °C. At this temperature, the sample is in the fluid state with a rather low viscosity. The cone-and-plate geometry was filled by means of a graduated pipet (Eppendorf, Germany). After equilibration at 20 °C for approximately half an hour, respectively, the measurement was started.

For the temperature-dependent screening of the dynamic moduli, a frequency of 1 Hz, a strain of 1%, and a heating rate of 0.1 K s^{-1} were applied. Data points were recorded every 2 s. The steady shear sweep experiment was performed at a constant temperature of 20 °C. The flow curves were measured in CSR mode (shear rate controlled measurement) with shear rates $\dot{\gamma}$ given logarithmically in the range between 1 and 10^3 s^{-1} with 10 data points per decade. The measuring time per data point was set automatically by the rheometer software based on the accuracy of the raw data. The measurement time of one flow curve was about 480 s. All measurements were repeated twice using the same sample.

Small-Angle Neutron Scattering (SANS). The presented SANS investigations were performed using the PAXY instrument of the Laboratoire Léon Brillouin (LLB, Saclay, France). A neutron

Scheme 2. Schematic Depiction of the Setup Used for the Rheo-SANS Measurements, Applying a Couette Shear Cell Geometry[a]

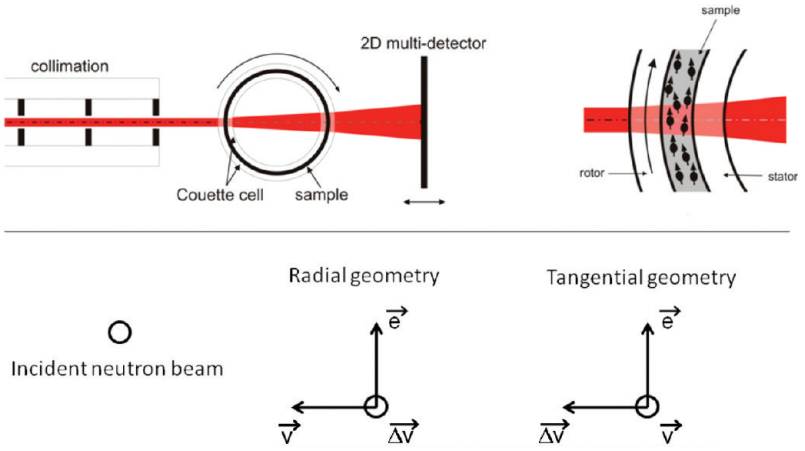

[a] $\vec{v}$ = velocity vector, $\Delta\vec{v}$ = shear gradient vector, and $\vec{e}$ = vorticity vector.

wavelength of $\lambda = 6$ Å with a spread of $\Delta\lambda/\lambda = 10\%$ and a sample-to-detector distance of 6.798 m was selected, covering the q-range of interest. Spherical sample apertures of 5 mm (radial) and 3 mm (tangential) were used. All samples were prepared in pure D_2O providing a good scattering contrast. The temperature of the sample was controlled by a thermostat to 20 ± 1 °C.

The cell for rheological measurements as well as the scattering geometry is presented in Scheme 2. The custom-made shear cell is built from quartz glass and consists of two cylindrical vessels (Couette cell type), an inner stator ($D = 45$ mm) and an outer rotator ($D = 47$ mm). The gap between the stator and rotator is ca. 1 mm. The shear cell could be moved along the direction perpendicular to the incident neutron beam. Hence, we were able to measure in radial (neutron beam perpendicular to the velocity vector $\vec{v}$, the shear direction) as well as in tangential scattering geometry (neutron beam parallel to the velocity vector). The outer rotator of the cell could be rotated at variable speed, inducing a changeable shear force. As a result, the slowest flow appears close to the inner wall, and the fastest close to the outer wall of the Couette cell.

Special care was taken while filling the shear cell. First, the inner stator was removed, and the sample was filled slowly in the rotator avoiding the formation of air bubbles. Then, the stator was slowly placed in its final position. Initially, scattering profiles were taken without applying any shear. In case of anisotropic scattering patterns due to preshearing from the sample filling, the sample cell was heated to about 35 °C to reach the sol state,[23] and subsequently cooled down to room temperature again. After equilibration for approximately 1 h, recorded scattering patterns were isotropic, revealing the absence of any crystalline order. Intensity profiles were calculated by circularly averaging the corresponding 2D scattering patterns, including corrections accounting for electronic noise, detector efficiency, and empty cell scattering. Normalization of the data to an absolute scale has not been performed, since the data analysis did not require absolute intensity values. All performed treatments were done using software provided by the LLB. Further information on the data treatment procedure of the LLB can be found elsewhere.[44,45] Analysis of the anisotropic scattering data was basically carried out using the 2D detector images. A self-written program was used to evaluate the azimuthal intensities at specific q-regions.

Results and Discussion

Rheological Behavior under Steady Shear. Before discussing the results obtained from SANS measurements, we first address the rheological properties of a 19 wt % solution of $P2VP_{56}$-*b*-PEO_{410}-*b*-P(GME_{48}-*co*-EGE_{48}) at pH = 7. At this pH, the polymer chains are aggregated into core−shell−corona (CSC) micelles with a hydrophobic P2VP core (Scheme 1). As mentioned in the Introduction, these micelles can either pack regularly in a cubic lattice, or form an open association via reversible physical cross-linking at elevated temperatures caused by the thermo-sensitive corona. This behavior is demonstrated in Figure 1A, showing the temperature-dependent dynamic moduli of the sample exposed to oscillatory shear. Regions, where G' exceeds G'' are defined as gel state, whereas regions with $G'' > G'$ are consistent with a fluid like behavior. Consequently, we observe a gel−sol−gel transition upon temperature increase. First, a cubic packing exists, which "melts" at about 30 °C. Upon a further increase in temperature, the thermo-sensitive P(GME-*co*-EGE) corona blocks become insoluble at ca. 40 °C and a micellar network is formed. The aim of this work is to clarify the structure of the low temperature gel phase by recording 2D SANS patterns under steady shear. Consequently, we studied the shear rate dependence of the steady shear stress and viscosity within the low temperature gel phase. This will give us the opportunity to discuss structural features and transitions observed by SANS in context with the rheological behavior of the gel. The results of the shear rate sweep are shown in Figure 1B. Basically, two different regimes can be identified with increasing shear rate. Both exhibit a power law behavior with different exponents. For shear rates $\leq 60\ s^{-1}$ we detect $\sigma \propto \dot{\gamma}^{0.06}$, i.e., the shear stress is almost independent of the shear rate, or in other words the shear stress reaches a plateau value. Consequently, the viscosity decreases strongly with increasing shear rate following a power law of $\eta \propto \dot{\gamma}^{-0.94}$. This behavior is typical for physical gels consisting of regularly packed micelles. As an example, for a 20 wt % solution of PEO_{110} end-capped with octadecyl groups, viscosity follows a power law with an exponent of −0.83, which is even increasing at higher shear rates.[30] This strong shear thinning behavior, resembling qualitatively the behavior of strong shear thinning solids rather than the behavior of normal fluids,[46,47] originates from a structural reorganization process.[28,30,47,48] We will discuss this phenomenon in more detail within the following sections. For shear rates $> 60\ s^{-1}$, the stress plateau is left and the shear stress becomes shear rate dependent following a power law with an exponent of 0.56. In this regime structural reorganization is complete, and stress dissipation takes place through crystal layers slipping past each other.[39]

Unfortunately, we were not able to detect the onset of the observed stress plateau, due to limitations with respect to the minimum accessible shear rate for the used cylindrical shear cell geometry. Thus, the existence of a yield stress, which is

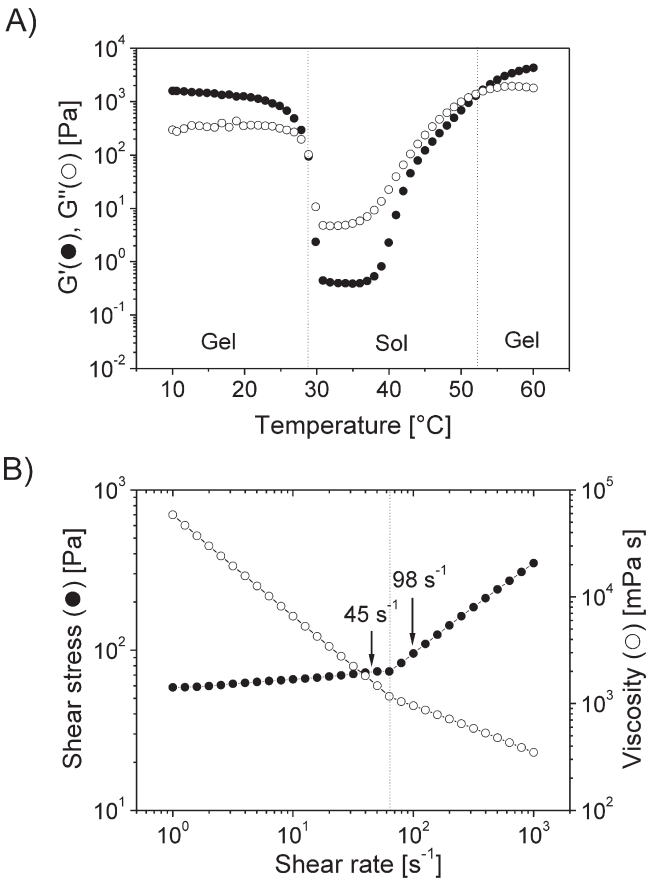

Figure 1. Rheological properties of a 19 wt % aqueous solution of $P2VP_{56}$-*b*-PEO_{410}-*b*-P(GME_{48}-*co*-EGE_{48}) at pH = 7: (A) temperature-dependent G' and G'' (0.1 K s^{-1}, 1 Hz, 1% strain); (B) shear stress and shear viscosity as a function of shear rate at 20 °C.

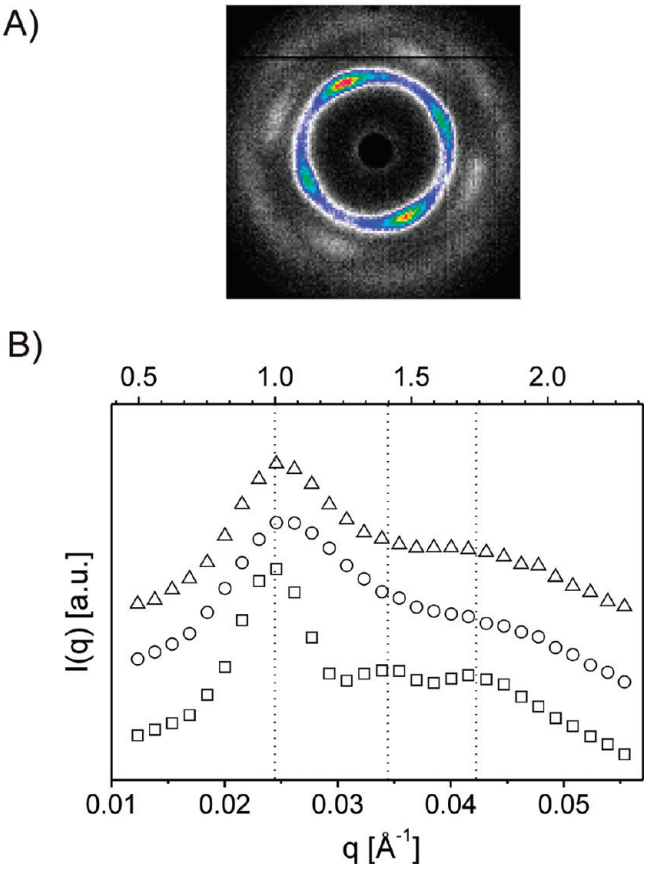

Figure 2. (A) 2D SANS pattern of a 19 wt % solution of $P2VP_{56}$-*b*-PEO_{410}-*b*-P(GME_{48}-*co*-EGE_{48}) at pH = 7 and T = 20 °C for radial scattering geometry, directly after filling the Couette cell. (B) Radially averaged static SANS profiles ($\dot{\gamma}$ = 0), immediately after loading the Couette cell (squares), at 35 °C (circles), and after cooling from 35 to 20 °C (triangles). The dashed vertical lines indicate the peak positions, which are in agreement with sc or bcc lattices.

expected for close packed micellar mesophases,[29,39,47−49] could not be verified with this setup. To address the question whether a yield stress exists for our system, we have switched to a cone-and-plate shear cell geometry, extending the measurement range to lower shear rates. The corresponding flow curve is shown in Figure S1 (Supporting Information), indicating a yield stress of about 10 Pa, and an onset of the stress plateau at a shear rate of 0.1 s^{-1}. However, in order to keep the comparability with the SANS experiments, which were performed using a Couette-type shear cell, the results obtained with the cylindrical shear cell geometry will be used for further discussion.

Small-Angle Neutron Scattering of a Nonsheared Sample. A crucial aspect of SANS experiments on concentrated micellar solutions is the effect of preshearing due to the filling of the sample cell. In our case, the 2D SANS image recorded right after filling the Couette cell at 20 °C shows a strong anisotropic character (Figure 2A). In the corresponding radially averaged intensity profile (Figure 2B), two well-defined higher order reflections can be detected, indicating a highly ordered state. The features of this SANS profile will be discussed later on in more detail. As shown in the Rheology section, the investigated sample undergoes a gel−sol transition at approximately 30 °C. As a result, the higher order reflections, found right after filling the Couette cell, vanish if the sample is heated to 35 °C (Figure 2B). Additionally, the position of the structure factor maximum (q_{max}) shifts toward higher values of q, and a broadening of the structure peak is observed. The shift of q_{max} to higher q values indicates a smaller center-to-center distance of the micelles. Thus, we can conclude that the temperature induced disintegration of the close micellar packing is caused by a shrinkage of the micelles, in accordance to our previous assumption.[23] This is consistent with the macroscopically observed gel−sol transition. If the sample is again cooled down to 20 °C and equilibrated for 1 h, q_{max} is shifted toward smaller values of q almost reaching its initial value directly after filling the cell. However, the structure peak at q_{max} is still broadened and no higher order reflections are visible. Only a plateau remains, originating from the form factor of the micelles.[23] Furthermore, the 2D scattering pattern has a purely isotropic character (not shown here). Consequently, the long-range order induced by the sample filling procedure is lost throughout the heating−cooling cycle. Therefore, every sample being under investigation in the following was subjected to a heating−cooling cycle prior to the measurements in order to eliminate any preshearing effects.

Nevertheless, the SANS pattern obtained at 20 °C right after filling the Couette cell provides first information on the structure of the gel, and can also be used for a comparison to our SANS results obtained for a P2VP-*b*-PEO-*b*-P(GME-*co*-EGE) triblock terpolymer exhibiting slightly different block lengths.[23] Compared to our previous findings, the position of the first order structure peak (q_{max}) is almost preserved and the same higher order reflections are visible, indicating that the type of crystal lattice is not altered and the lattice spacing is not considerably changed. The relative peak positions of the higher order reflections of $1:2^{1/2}:3^{1/2}$ are consistent with a

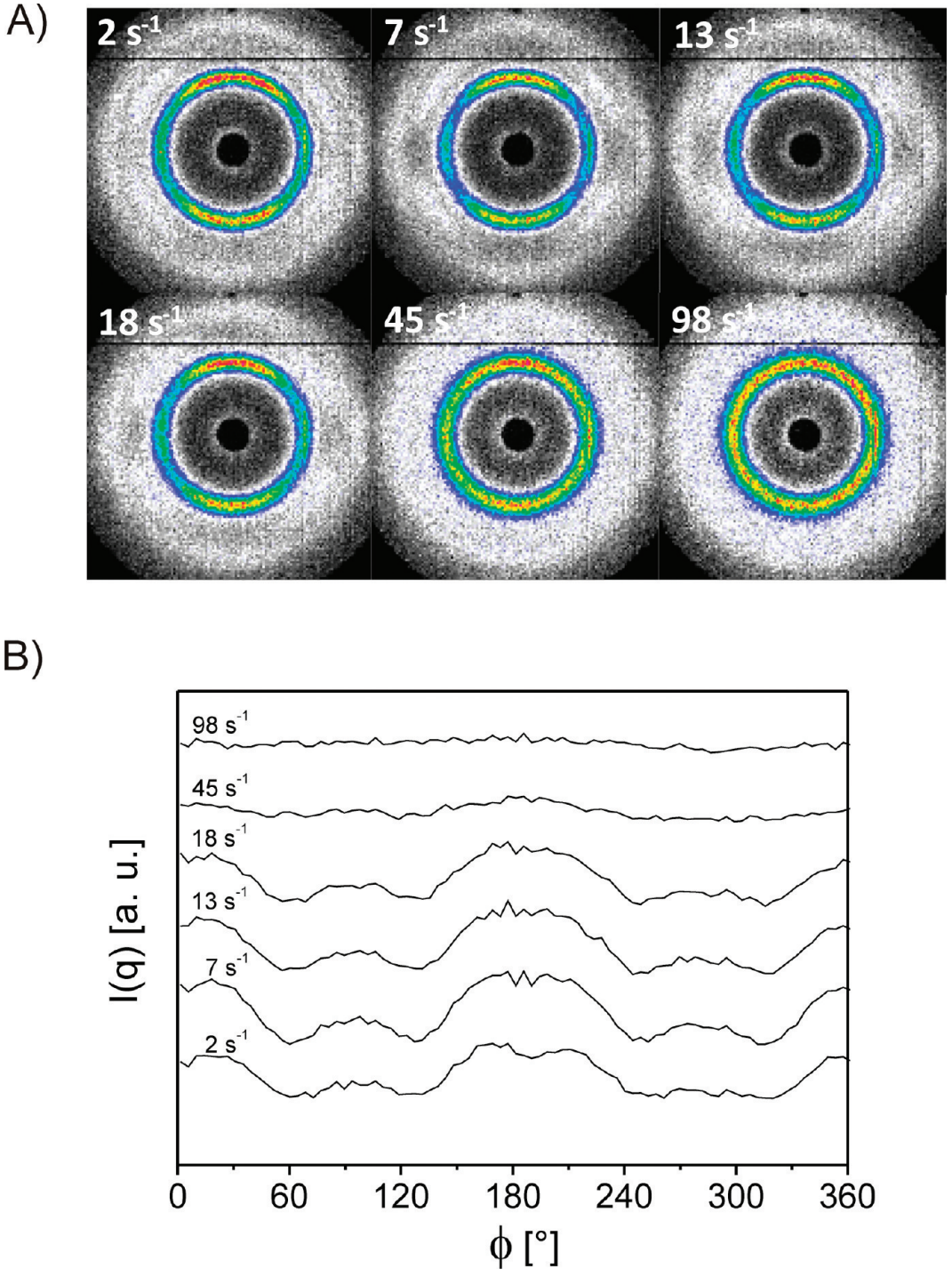

Figure 3. (A) 2D SANS patterns of a 19 wt % solution of $P2VP_{56}$-*b*-PEO_{410}-*b*-P(GME_{48}-*co*-EGE_{48}) at pH = 7 and $T = 20$ °C for radial scattering geometry, obtained during shear at different shear rates. (B) Azimuthal scattering intensities along the first Bragg ring (clockwise, starting from the southern meridian) calculated from the 2D SANS patterns shown in part A.

body centered cubic (bcc) or a simple cubic (sc) packing, but not with a fcc structure, where reflections should be located at relative peak positions of $1:4/3^{1/2}:8/3^{1/2}:11/3^{1/2}$.[50] Our results are consistent with the general prediction, that fcc lattices are unfavorable for micelles acting as "soft" spheres. For these systems the formation of bcc structures is frequently observed;[25−34] however, from our data the presence of a sc lattice cannot be excluded so far.

Small-Angle Neutron Scattering under Steady Shear. Figure 3A shows 2D scattering patterns recorded at different shear rates for radial scattering geometry (Scheme 2). Starting with the lowest shear rate of $2\ s^{-1}$, a continuous Bragg ring with strong reinforcements in the meridional position and weaker ones on the equatorial axis, as well as four relative diffuse, ellipsoidal reflexes at higher q values are visible. This indicates a polycrystalline structure with a weak preferential orientation of the crystal domains. Upon increasing the shear rate, the described pattern first becomes more defined but then more diffuse again. Finally, at a rate of $98\ s^{-1}$ the pattern is fully isotropic. Therefore, at a first glance it seems, that a weak order is induced upon exposing the sample to low shear rates. This order subsequently disappears again, when the shear rate exceeds a certain value. The same trend

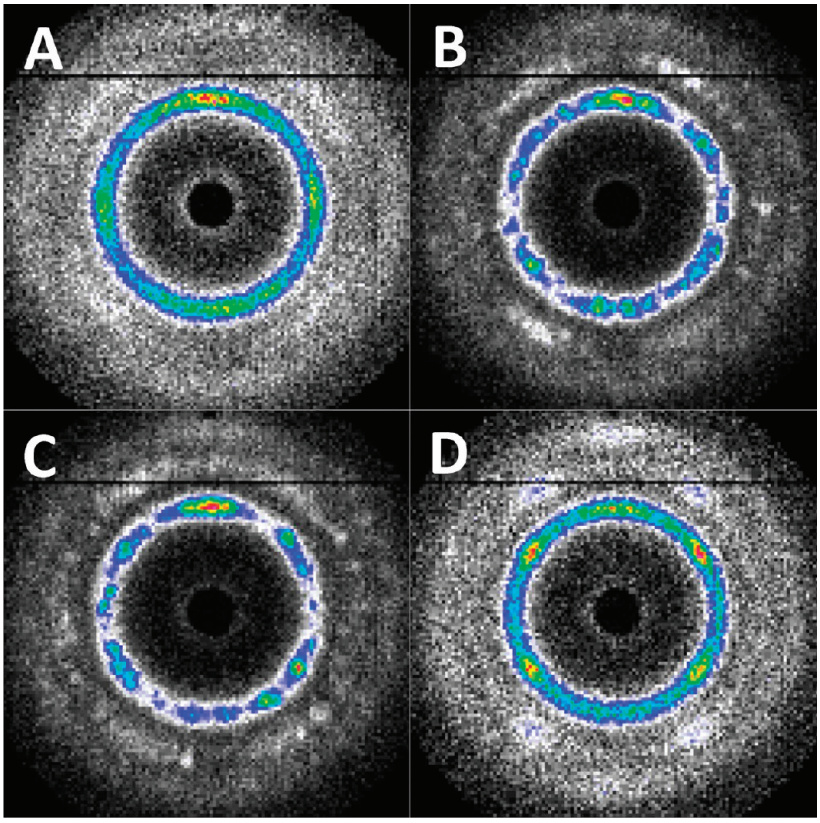

Figure 4. 2D SANS patterns of a 19 wt % solution of $P2VP_{56}$-*b*-PEO_{410}-*b*-P(GME_{48}-*co*-EGE_{48}) at pH = 7 and $T = 20$ °C for radial scattering geometry, obtained after cessation of shear at (A) 18 s^{-1}, (B) 45 s^{-1}, (C) 98 s^{-1}, and (D) 98 s^{-1} with a long period of preshearing (several hours).

is observed following the azimuthal evolution of the scattering intensity along the first Bragg ring, i.e., at a fixed value of $q = 0.24$ $Å^{-1}$ (Figure 3B).

In contrast, a completely different picture evolves, when scattering patterns are recorded right after the shear was stopped. At low shear rates (< 18 s^{-1}), the low degree of ordering vanishes after cessation of the shear (not shown here). At higher shear rates (≥ 18 s^{-1}), the anisotropy is preserved and becomes even more pronounced (Figure 4). This is consistent with the common observation that the alignment process becomes irreversible upon exceeding a critical shear rate.[27,28,41] Finally, the fully isotropic pattern, obtained during shear at high rates (98 s^{-1}), develops into a strong anisotropic pattern with sharp Bragg spots after cessation of the shear (Figure 4C,D). However, the Bragg spots in Figure 4, parts B and C, are rather grainy with weakly defined positions, indicating a rather ill-defined alignment. This is due to the fact, that the shearing process during the shear rate screening was interrupted several times in order to record scattering patterns from the quiescent state for each applied shear rate. A really defined pattern, represented in Figure 4D, is only obtained when the sample is sheared continuously without any interruption for several hours.

The fact, that the structural order is generally less pronounced during shear, is most probably related to the soft character of the studied CSC micelles.[23] The relatively large, soft shell might be easily deformed by mechanical stress. As a consequence, the number of defects in the crystal domains increases, which affects the degree of long-range structural order under shear. Watanabe et al. observed a similar behavior for a 15 wt % solution of a PS_{106}-*b*-PB_{426} diblock copolymer in *n*-tetradecane. When shear was switched off, the obtained patterns became more defined as well.[49] However, regarding hydrogels based on a close cubic packing of micelles, scattering patterns presented in literature are mostly obtained under steady shear, and a shear-induced disordering at moderate shear rates has not been reported so far. In one particular contribution, dealing with a PEO_{76}-*b*-PPO_{29}-*b*-PEO_{76} (Pluronics F68) solution, the authors note that small-angle X-ray scattering (SAXS) patterns at any given shear rate and after cessation of shear are identical.[28] Despite, there are reports on shear-induced disordering in block copolymer melts or highly concentrated block copolymer solutions at temperatures close to the order−disorder transition (ODT).[51−54] Interestingly, after cessation of shear the shear-induced disorder vanished again. For a highly oriented twinned bcc structure a complete destruction of the ordered melt phase was observed at intermediate shear rates, however, after cessation of shear the initial twinned bcc structure was recovered completely.[53] This is quite similar to our observations. The apparent disordering during steady shear was explained by an increasing number of defects being introduced above a certain shear rate. When the defects are generated faster than they can move or be annihilated by slipping, the translational order between crystal layers is lost resulting in the observed isotropic scattering pattern. However, the orientational order is retained, i.e. after cessation of shear the layers can easily restack and reestablish the crystalline order.

The deformability of a micelle should strongly depend on the absolute size of the micellar shell, expressed by the overall average degree of polymerization (DP_{shell}), and its relative size with respect to that of the core forming block, expressed by the DP_{shell}:DP_{core} ratio. The higher both values, the easier the shear-induced deformation of the micelles should take place. It appears, that in most reports on micellar hydrogels either the relative shell size or the absolute size is lower compared to our system ($DP_{PEO\text{-}b\text{-}P(GME\text{-}co\text{-}EGE)}$:$DP_{P2VP}$ = 9:1; $DP_{PEO\text{-}b\text{-}P(GME\text{-}co\text{-}EGE)}$ = 506). Consequently, the

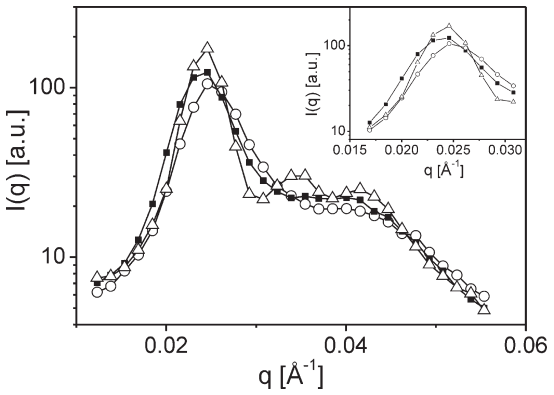

Figure 5. Radially averaged SANS profiles for a 19 wt % solution of P2VP$_{56}$-*b*-PEO$_{410}$-*b*-P(GME$_{48}$-*co*-EGE$_{48}$) at pH = 7 and T = 20 °C before (circles), during (squares), and after (triangles) exposure to a shear rate of 98 s^{-1}. The inset shows an enlargement of the q-range corresponding to the first order structure peak.

shear-induced disordering observed for P2VP-*b*-PEO-*b*-P(GME-*co*-EGE) based hydrogels for shear rates >18 s^{-1} is most probably attributed to defects induced by a significant deformation of the micellar shell, which results in a decrease of the translational order between the crystal layers.

The deformation of the CSC micelles can be verified by comparing the positions of the structure factor maximum in the radially averaged intensity profiles obtained under shear and after cessation of shear, respectively (Figure 5). Under shear, the peak maximum is located at slightly lower q values compared to the sample, which was not subjected to shear before. This phenomenon can only be explained by a deformation of the spherical micelles, causing a change in the average center-to-center distance, as expressed by the shift of the peak maximum. Additionally, the structure factor peak is slightly broadened, which is consistent with an overall less defined arrangement of the micelles. An analogous behavior was described by Stellbrink et al. for a poly(ethylene-*co*-propylene)-*block*-poly(ethylene oxide) (PEP$_{15}$-*b*-PEO$_{497}$) diblock copolymer.[46] After cessation of shear, q_{max} is shifted back to the initial position, indicating that this process is reversible, i.e., the original spherical shape of the micelles is recovered (Figure 5). The reversibility can be understood, if we keep in mind that the core of the micelles is composed of fully collapsed, glassy poly(2-vinylpyridine), which is more or less unaffected by moderate mechanical stress, and therefore forces the micellar shell back to its original shape after cessation of shear.

Some first conclusions can be drawn from the results obtained so far. Upon increasing the shear rate, a structural reorganization from a fully polycrystalline to a polycrystalline structure with a weak preferential orientation takes place, becoming irreversible at shear rates ≥ 18 s^{-1}. At even higher shear rates (>45 s^{-1}), a second transition to a more defined structural alignment occurs. When patterns are recorded under steady shear, structural reorganization is overlapped by a reversible deformation of the micelles, decreasing the degree of long-range structural order. It is noted, that the initial SANS results can nicely be related to the findings from rheological measurements. All shear rates at which 2D patterns were recorded, except the highest one, are located in the region where the stress plateau was observed (Figure 1B). Therefore, this stress plateau is clearly correlated with structural reorganization processes. The highest shear rate applied (98 s^{-1}) is already located outside the stress plateau, which indicates that the reorganization process is more or less completed at that point. In the corresponding scattering pattern (Figure 4D), relatively sharp Bragg spots are observed, which is typical for a defined long-range structural alignment. However, a full alignment of the whole sample is not achieved even at 98 s^{-1}, as evidenced by the superposition of the Bragg spots with a continuous Bragg ring. This might indicate the existence of some remaining nonoriented polycrystalline domains. In radial scattering geometry, the incident neutron beam is parallel to the shear gradient vector $\Delta\vec{v}$ and therefore passes all different states of orientation (Scheme 2). It is obvious, that different states of alignment might occur along this shear gradient axis, due to the fact that the flow next to the outer wall of the cell (rotator) is relatively fast, whereas the crystal domains next to the inner wall (stator) are almost at rest. Nevertheless, the abrupt change of the power law exponents for the shear rate dependent shear stress and viscosity at around 60 s^{-1} indicates, that stress dissipation is not longer dominated by structural reorganization but rather by slipping of crystal layers, i.e., the sample is almost fully aligned.

In the last section, the 2D SANS patterns are analyzed in more detail in order to derive information about the exact crystal lattice and macroscopic alignment of the hydrogel. The main feature of the pattern observed after shearing at a shear rate of 18 s^{-1} (Figure 4A) is the existence of a continuous inner Bragg ring with significantly reinforced scattering at the meridional positions, and weaker scattering at the equatorial positions. As already mentioned, the continuous Bragg ring points to the presence of a nonoriented, polycrystalline texture. However, the higher scattering intensity at the meridional positions of the inner Bragg ring indicates a weak preferential orientation of the domains. In agreement with the results of Hamley et al.,[40,41] the observed pattern corresponds to a bcc structure, with the pair of meridional reflections originating from {110} planes oriented perpendicular to the $\vec{v}$, $\vec{e}$ shear plane. The polydomain nature of the structure is further verified by the fact, that weak equatorial {110} reflections are present as well. Since no monodomain bcc structure leading to such a pattern exists, it must represent differently oriented domains. The diffuse Bragg spots on the second ring, i.e., corresponding to the {200} reflections, enclose an angle of 45° with the meridional {110} reflections. Hence, they originate from the same oriented bcc domain.

We now turn to the scattering pattern obtained after shearing at a rate of 98 s^{-1}. Easiest stress dissipation in the case of fully aligned domains is accomplished by layer-by-layer slipping of specific planes, oriented parallel to the shear plane, and with the most closely packed direction being aligned along the shear direction.[55] In bcc crystal lattices the [111] direction is the most densely packed one, and the energetically most favored slipping plane is the {110} plane. Alternative slipping planes are the {211} and {321} planes, although they are energetically less favored. Eiser et al. investigated a 46 wt % solution of PEO$_{76}$-*b*-PPO$_{29}$-*b*-PEO$_{76}$ (Synperonic F68),[28] observing a scattering pattern strongly resembling the pattern obtained in our study after cessation of shear at 98 s^{-1} (Figure 6A). By increasing the shear rate to a very high value of 365 s^{-1}, however, the meridional reflections on the first Bragg ring vanished. This phenomenon went along with a second stress plateau, indicating a second structural reorganization process. The remaining spots, marked in red in the theoretical scattering pattern (Figure 6B), were assigned to a fully oriented twinned bcc monodomain, with the [111] direction being oriented parallel to the flow direction and the energetically most favored {110} planes being exclusively stacked parallel to the shear plane, as predicted. It is noted, that we do not observe the reflections on the third ring located around the equator. This is probably due to a poor contrast as a consequence of the relatively low neutron flux in the present

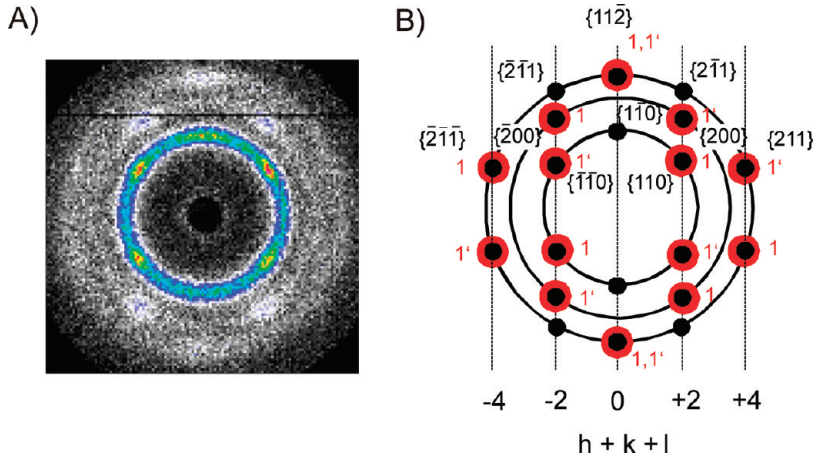

Figure 6. (A) 2D SANS pattern of a 19 wt % solution of P2VP$_{56}$-*b*-PEO$_{410}$-*b*-P(GME$_{48}$-*co*-EGE$_{48}$) at pH = 7 and T = 20 °C for radial scattering geometry, obtained after cessation of shear at 98 s^{-1} with a long period of preshearing. (B) Theoretical diffraction pattern for a bcc structure oriented with the [111] direction in flow direction according to Perreur et al. and Hamley et al. for radial geometry (black spots),[27,41,57] and expected diffraction pattern for a homogeneously oriented twinned bcc structure with the [111] direction in flow direction and the {110} planes parallel to the shear plane (red spots).[28]

experiments. By recording scattering patterns in tangential scattering geometry, Eiser et al. could conclude that the additional meridional spots on the first Bragg ring observed at intermediate shear rates (which we also observe) originated from twinned bcc monodomains as well, but tilted by an angle of 90° around the velocity axis. In consequence, these domains were oriented with their {211} planes parallel and their {110} planes perpendicular to the shear plane. It was shown, that the differently oriented domains were separated from each other along the shear gradient axis $\Delta\vec{v}$. Close to the outer cell wall (rotator), where the shear velocity was the highest, domains with the densely packed {110} slipping planes oriented parallel to the Couette walls were formed, since these planes provide easiest stress dissipation. On the other hand, domains with the {211} slipping planes being oriented parallel to the Couette walls, which is energetically less favored, consequently were located more or less in the middle of the cell gap where the shear velocity was lower. A similar dependence of the orientation of twinned bcc crystals on the applied shear was found by Mortensen for organogels based on polystyrene-*block*-poly(ethylene-*co*-butylene)-*block*-polystyrene (PS-*b*-PEB-*b*-PS) triblock copolymers.[56] Since the neutron beam we used was wider than the gap of the measuring cell, we were not able to verify the separation of the different orientations along the shear gradient axis by performing measurements in tangential geometry in our case. However, we should at least observe a superposition of the patterns of the two different orientations analogous to the measurements in radial geometry.

First of all, we observe a weak continuous Bragg ring probably originating from some nonoriented polydomains next to the inner Couette wall (stator) (Figure 7A). In addition, a hexagonal array of Bragg spots is observed. This is consistent with the tangential scattering pattern obtained by Eiser et al. for the fully aligned twinned bcc domains with {110} planes parallel to the shear plane, i.e., walls of the Couette cell.[28] Moreover, a second set of hexagonally distributed Bragg spots being rotated by 90° relative to the first hexagon, as it is expected for domains with {211} slipping planes being oriented parallel to the shear plane, should occur as well. We do not observe such a feature, which might be attributed to the fact that the corresponding meridional reflections in radial scattering geometry are relatively weak; i.e., the majority of domains is oriented with the {110} planes parallel to the shear

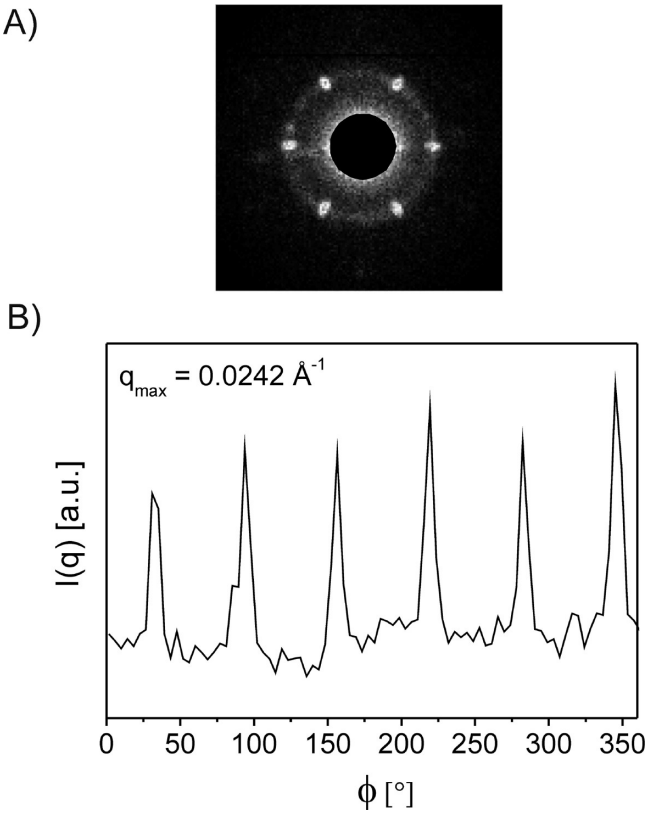

Figure 7. (A) 2D SANS pattern of a 19 wt % solution of P2VP$_{56}$-*b*-PEO$_{410}$-*b*-P(GME$_{48}$-*co*-EGE$_{48}$) at pH = 7 and T = 20 °C for tangential scattering geometry, obtained after cessation of shear at 98 s^{-1} with a long period of preshearing. (B) Corresponding plot of the scattering intensity of the Bragg spots on the first Bragg ring as a function of the azimuthal angle (clockwise, starting from the southern meridian).

plane. This finding is supported by rheology, showing that the structural reorganization process is more or less completed at 98 s^{-1}, having in mind that the {110} orientation parallel to the shear plane is the final most stable state of alignment.

Consequently, the scattering pattern in Figure 6A can be explained in a satisfying way by considering the presence of twinned bcc monodomains with two different preferred

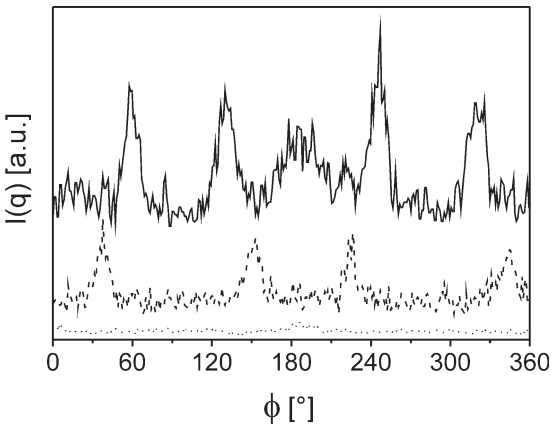

Figure 8. Intensity of reflections located on different rings of constant q values as a function of the azimuthal angle (clockwise, starting from the southern meridian) calculated from Figure 6A: $q_{max,1} = 0.0244$ Å^{-1} (solid), $q_{max,2} = 0.0348$ Å^{-1} (dashed), and $q_{max,3} = 0.0416$ Å^{-1} (dotted).

orientations. Nevertheless, the scattering pattern might also be explained without considering the presence of a twinned structure. In order to orient the favored {110} slipping planes parallel to the shear plane, the domains can be rotated around the [111] direction by two different angles. The resulting pattern, which consequently is a superposition of two single patterns, is identical with the one observed for the corresponding twinned structure (red spots in Figure 6B).[41,57] The black spots in Figure 6B represent the theoretical pattern, which arises when the domains are rotated around the [111] direction by all eight possible angles, i.e., any angle for which one of the three energetically favored slipping planes ({110}, {211}, {321}) are oriented parallel to the shear plane.[27,41,57] The pattern in Figure 6A does not match exactly with this theoretical pattern, since the {211} reflections next to the meridian are missing. However, neither Perreur et al. nor Eiser et al. were able to detect the {211} reflection near the meridian, which indicates that it is rather unfavorable for the domains to orient with the {321} planes parallel to the shear plane.[27,28] This is reasonable, since the {321} planes are the energetically least favored slipping planes.

What we can conclude so far is that the position of the Bragg spots in Figure 6A at least fully corresponds to a bcc structure with the [111] direction oriented parallel to the flow direction. An additional procedure of proving the nature of the network and its preferred orientation direction is also given by Perreur et al.[27] The indices $\{hkl\}$ of the spots on the pattern all follow the relation $uh + vk + wl = n$. Spots with the same order n lie on the same vertical axis in the 2D pattern. All axes are equidistant to each other, separated by a gap Δ. If we deal with bcc crystals oriented around the [111] direction, the radius of the first Bragg ring in the SANS pattern (r_1) divided by Δ should give a value of 1.22. In our case, we determine a value of 1.21, which is in good agreement with the theoretical prediction.

We now still have to address the question whether we deal with a twinned bcc structure or not. The distribution of the Bragg spots in the radial scattering pattern of the shear oriented sample (Figure 6A) can be fully explained by both scenarios (see discussion above). However, a twinned structure would require equal intensities of all Bragg spots appearing on the first ring in the pattern, except for the meridional ones. When having a look at the scattering intensity of the Bragg spots on the first ring as a function of the azimuthal angle Φ, this requirement seems to be fulfilled for radial geometry in good approximation, though the general signal-to-noise ratio is relatively low (Figure 8). A similar behavior is observed for the tangential scattering geometry. A closer look to the intensity of the Bragg spots (Figure 7B) implies the existence of two sets of intensities, as only spots separated by an angle of 120° exhibit the same intensity. This in turn would be contradictory to a twinned bcc structure. However, within the accuracy of the experiment, the intensities of the different Bragg spots are identical. In conclusion, the shear-oriented sample (shear rate 98 s^{-1}) most likely exhibits an almost fully aligned twinned bcc structure with the {110} planes oriented parallel to the shear plane. Nevertheless, the presence of non-twinned bcc domains exhibiting different orientations with respect to the [111] axis cannot completely be ruled out.

Finally, we still need to discuss the patterns obtained at shear rates of 45 and 98 s^{-1}after a stepwise increase of the shear rate, i.e., in this case the sample was not continuously presheared at a given shear rate prior to the measurement (Figure 4B,C). Both patterns exhibit an irregular distribution of the Bragg spots. It is obvious, that the [111] axis of the bcc domains in these cases is not fully aligned in direction of the shear. A small tilt of the [111] axis of some of the domains causes a shift of the angle for which the Bragg relation is fulfilled. However, we observe irregularly distributed Bragg spots and not continuous banana-like patterns of high intensity, as observed in Figure 4A. This indicates, that in contrast to a polydomain structure, the fraction of domains exhibiting a defined orientation of the [111] axis with respect to the shear direction is comparatively large.

Conclusion

A 19 wt % aqueous solution of P2VP$_{56}$-*b*-PEO$_{410}$-*b*-P(GME$_{48}$-*co*-EGE$_{48}$), forming a free-standing gel at pH = 7 and room temperature, was exposed to steady shear in order to induce a macroscopic alignment of the crystal domains, enabling the assignment of the exact structure of the micellar packing by SANS. Higher order reflections at relative peak positions of 1: $2^{1/2}$: $3^{1/2}$ in the radially averaged SANS intensity profile of a presheared sample indicated the presence of either a simple cubic (sc), or body centered cubic (bcc) lattice.

Upon exposure to steady shear, the sample exhibited a stress plateau at shear rates below 60 s^{-1}, i.e., a strong shear thinning behavior was found. Small-angle neutron scattering experiments at different shear rates revealed, that the existence of this plateau is due to two different structural transitions. First, a transition from a fully nonoriented polydomain to a polydomain with weak preferential orientation occurred at intermediate shear rates. Subsequently, at the end of the stress plateau a macroscopic alignment was observed, where flow is provided by different crystal layers slipping past each other. The latter highly aligned structure was identified as a twinned bcc lattice, with a major fraction of the crystal domains oriented with the [111] direction in shear direction, and the {110} slipping planes parallel to the shear plane. A small fraction, most probably located close to the inner wall (stator) of the Couette cell, was oriented with the {110} planes perpendicular to the shear plane. This is consistent with literature data, showing that the perpendicular alignment is preferentially formed for moderate shear rates. It is noted, that at the highest applied shear rate of 98 s^{-1} still nonoriented polydomains are detectable, indicating that the alignment is incomplete. This is due to the velocity gradient along the gap of the used Couette shear cell. A fully oriented sample might be achievable at very high shear rates, which were not accessible in our case.

Finally, we observed that the structural transitions induced by shear are irreversible for shear rates higher than 18 s^{-1}. Furthermore, the shape of the micelles is distorted during shear due to their relatively large and soft shell, which lowers the degree of

structural order. This results in an apparent shear-induced disordering at moderate shear rates, as the corresponding 2D scattering pattern became isotropic under shear. However, upon cessation of shear a highly anisotropic pattern evolved, indicating that the shear-induced distortion of the micellar shell is fully reversible.

Acknowledgment. The authors acknowledge the German Science Foundation (priority program SPP 1259) for financial support. M.K. is grateful to the Alexander von Humboldt foundation for a Feodor-Lynen research fellowship. The SANS experiments were partially supported by the European Union within the framework of the NMI3 program.

Supporting Information Available: Flow curve obtained using a cone-and-plate shear cell geometry and corresponding discussion of the results. This material is available free of charge via the Internet at http://pubs.acs.org.

References and Notes

(1) Tachibana, Y.; Kurisawa, M.; Uyama, H.; Kakuchi, T.; Kobayashi, S. *Chem. Lett*. **2003**, *32*, 374–375.
(2) Hart, D. S.; Gehrke, S. H. *J. Pharm. Sci*. **2007**, *96*, 484–516.
(3) Yu, L.; Ding, J. *Chem. Soc. Rev*. **2008**, *37*, 1473–1481.
(4) Ahn, S.-k.; Kasi, R. M.; Kim, S.-C.; Sharma, N.; Zhou, Y. *Soft Matter* **2008**, *4*, 1151–1157.
(5) He, C.; Kim, S. W.; Lee, D. S. *J. Controlled Release* **2008**, *127*, 189–207.
(6) Klouda, L.; Mikos, A. G. *Eur. J. Pharm. Biopharm*. **2008**, *68*, 34–45.
(7) Beebe, D. J.; Moore, J. S.; Bauer, J. M.; Yu, Q.; Liu, R. H.; Devadoss, C.; Jo, B.-H. *Nature* **2000**, *404*, 588–590.
(8) Calvert, P.; Patra, P.; Duggal, D. *Proc. SPIE-Int. Soc. Opt. Eng*. **2007**, *6524*, 65240M/1–65240M/6.
(9) Guenther, M.; Kuckling, D.; Corten, C.; Gerlach, G.; Sorber, J.; Suchaneck, G.; Arndt, K. F. *Sens. Actuators, B* **2007**, *126*, 97–106.
(10) Dai, S.; Ravi, P.; Tam, K. C. *Soft Matter* **2008**, *4*, 435–449.
(11) Jindrich, K. *J. Polym. Sci., Part A: Polym. Chem*. **2009**, *47*, 5929–5946.
(12) Lin, H.-H.; Cheng, Y.-L. *Macromolecules* **2001**, *34*, 3710–3715.
(13) Fechler, N.; Badi, N.; Schade, K.; Pfeifer, S.; Lutz, J.-F. *Macromolecules* **2008**, *42*, 33–36.
(14) Bae, S. J.; Joo, M. K.; Jeong, Y.; Kim, S. W.; Lee, W.-K.; Sohn, Y. S.; Jeong, B. *Macromolecules* **2006**, *39*, 4873–4879.
(15) Shinji, S.; Shokyoku, K.; Sadahito, A. *J. Polym. Sci., Part A: Polym. Chem*. **2004**, *42*, 2601–2611.
(16) Iddon, P. D.; Armes, S. P. *Eur. Polym. J*. **2007**, *43*, 1234–1244.
(17) Sotirios, A. A.; Constantinos, T. *Macromol. Chem. Phys*. **2006**, *207*, 2188–2194.
(18) Dayananda, K.; Pi, B. S.; Kim, B. S.; Park, T. G.; Lee, D. S. *Polymer* **2007**, *48*, 758–762.
(19) Nikoletta, S.; Ilias, K.; Sotirios, A.; Constantinos, T. *Macromol. Rapid Commun*. **2008**, *29*, 130–135.
(20) Hadjiantoniou, N. A.; Patrickios, C. S. *Polymer* **2007**, *48*, 7041–7048.
(21) Achilleos, M.; Krasia-Christoforou, T.; Patrickios, C. S. *Macromolecules* **2007**, *40*, 5575–5581.
(22) Xu, F.-J.; Kang, E.-T.; Neoh, K.-G. *Biomaterials* **2006**, *27*, 2787–2797.
(23) Reinicke, S.; Schmelz, J.; Lapp, A.; Karg, M.; Hellweg, T.; Schmalz, H. *Soft Matter* **2009**, *5*, 2648–2657.
(24) Ah Toy, A.; Reinicke, S.; Müller, A. H. E.; Schmalz, H. *Macromolecules* **2007**, *40*, 5241–5244.
(25) Hamley, I. W.; Daniel, C.; Mingvanish, W.; Mai, S.-M.; Booth, C.; Messe, L.; Ryan, A. J. *Langmuir* **2000**, *16*, 2508–2514.
(26) McConnell, G. A.; Gast, A. P.; Huang, J. S.; Smith, S. D. *Phys. Rev. Lett*. **1993**, *71*, 2102–2105.
(27) Perreur, C.; Habas, J.-P.; François, J.; Peyrelasse, J.; Lapp, A. *Phys. Rev. E* **2002**, *65*, 041802/1–041802/7.
(28) Eiser, E.; Molino, F.; Porte, G.; Diat, O. *Phys. Rev. E* **2000**, *61*, 6759–6764.
(29) Eiser, E.; Molino, F.; Porte, G.; Pithon, X. *Rheol. Acta* **2000**, *39*, 201–208.
(30) Nicolai, T.; Benyahia, L. *Macromolecules* **2005**, *38*, 9794–9802.
(31) Tan, H.; Watanabe, H. *Polym. J*. **2004**, *36*, 430–434.
(32) Sebastian, J. M.; Lai, C.; Graessley, W. W.; Register, R. A. *Macromolecules* **2002**, *35*, 2707–2713.
(33) Park, M. J.; Char, K.; Bang, J.; Lodge, T. P. *Macromolecules* **2005**, *38*, 2449–2459.
(34) Gast, A. P. *Langmuir* **1996**, *12*, 4060–4067.
(35) Fleischer, G.; Rittig, F.; Kärger, J.; Papadakis, C. M.; Mortensen, K.; Almdal, K.; Stepanek, P. *J. Chem. Phys*. **1999**, *111*, 2789–2796.
(36) Higgins, J. S.; Dawkins, J. V.; Maghami, G. G.; Shakir, S. A. *Polymer* **1986**, *27*, 931–936.
(37) Watanabe, H.; Kotaka, T.; Hashimoto, T.; Shibayama, M.; Kawai, H. *J. Rheol*. **1982**, *26*, 153–179.
(38) Hamley, I. W.; Pople, J. A.; Fairclough, J. P. A.; Terrill, N. J.; Ryan, A. J.; Booth, C.; Yu, G. E.; Diat, O.; Almdal, K.; Mortensen, K.; Vigild, M. *J. Chem. Phys*. **1998**, *108*, 6929–6936.
(39) McConnell, G. A.; Lin, M. Y.; Gast, A. P. *Macromolecules* **1995**, *28*, 6754–6764.
(40) Hamley, I. W.; Pople, J. A.; Booth, C.; Derici, L.; Impéror-Clerc, M.; Davidson, P. *Phys. Rev. E* **1998**, *58*, 7620–7628.
(41) Hamley, I. W.; Pople, J. A.; Booth, C.; Yang, Y. W.; King, S. M. *Langmuir* **1998**, *14*, 3182–3186.
(42) Jiang, J.; Burger, C.; Li, C.; Li, J.; Lin, M. Y.; Colby, R. H.; Rafailovich, M. H.; Sokolov, J. C. *Macromolecules* **2007**, *40*, 4016–4022.
(43) Schmidt, G.; Richtering, W.; Lindner, P.; Alexandridis, P. *Macromolecules* **1998**, *31*, 2293–2298.
(44) Brulet, A.; Lairez, D.; Lapp, A.; Cotton, J.-P. *J. Appl. Crystallogr*. **2007**, *40*, 165–177.
(45) Cotton, J. P. Initial Data Treatment. In *Neutron X-Ray and Light Scattering*; Lindner, P., Zemb, T., Eds.; Elsevier Science Publishers B. V.: Amsterdam, 1991.
(46) Stellbrink, J.; Lonetti, B.; Rother, G.; Willner, L.; Richter, D. *J. Phys.: Condens. Matter* **2008**, 404206/1–404206/9.
(47) Prud'homme, R. K.; Wu, G.; Schneider, D. K. *Langmuir* **1996**, *12*, 4651–4659.
(48) Singh, M.; Agarwal, V.; De Kee, D.; McPherson, G.; John, V.; Bose, A. *Langmuir* **2004**, *20*, 5693–5702.
(49) Watanabe, H.; Kanaya, T.; Takahashi, Y. *Macromolecules* **2001**, *34*, 662–665.
(50) Huang, Y.-Y.; Chen, H.-L.; Hashimoto, T. *Macromolecules* **2003**, *36*, 764–770.
(51) Balsara, N. P.; Dai, H. J. *J. Chem. Phys*. **1996**, *105*, 2942–2945.
(52) Di Cola, E.; Fleury, C.; Panine, P.; Cloitre, M. *Macromolecules* **2008**, *41*, 3627–3635.
(53) Koppi, K. A.; Tirell, M.; Bates, F. S. *J. Rheol*. **1994**, *38*, 999–1027.
(54) Wang, H.; Kesani, P. K.; Balsara, N. P.; Hammouda, B. *Macromolecules* **1997**, *30*, 982–992.
(55) Ackerson, B. J.; Clark, N. A. *Phys. Rev. A* **1984**, *30*, 906–918.
(56) Mortensen, K. *J. Polym. Sci., Part B: Polym. Phys*. **2004**, *42*, 3095–3101.
(57) Hamley, I. W.; Pople, J. A.; Fairclough, J. P. A.; Ryan, A. J.; Booth, C.; Yang, Y. W. *Macromolecules* **1998**, *31*, 3906–3911.